

Understanding Galactic disk morphology through open star clusters and surrounding interstellar material

Y. C. Joshi^{1***}, Sagar Malhotra²

¹Aryabhata Research Institute of Observational Sciences (ARIES), Manora Peak, Nainital 263002, India

²Indian Institute of Science Education & Research, Mohali 140306, India

Preprint online version: December 20, 2022

Abstract

Context. The understanding of the Milky Way has progressed immensely after the release of the Gaia survey data. Thousands of new open clusters are detected and physical parameters are derived using precise photometric and kinematic information available for more than a billion sources in the Gaia archive.

Aims. As Open clusters are excellent sources to probe the structural details of the Galactic disk, we aim to use the largest open clusters catalogue compiled in the post-Gaia era to understand the Galactic disk morphology.

Methods. By compiling the physical parameters available for more than 6000 open clusters like age, distance, reddening, and kinematic information, we study the spatial distribution of the open clusters in the Galactic disk and analyse the distribution of interstellar material in the solar neighbourhood.

Results. Using the young open clusters as a tracer of spiral arms, we map the spiral structure of the Galaxy and found that most of the clusters leave the spiral arms after about 10-20 Myr and fill the inter-arm regions as they age. We determine the spiral pattern rotation speed of the Galaxy $\Omega = 26.5 \pm 1.5 \text{ km s}^{-1} \text{ kpc}^{-1}$, which is found to be constant within last ~ 80 Myr, and the corotation radius $R_c = 1.08^{+0.06}_{-0.05} R_\odot$. Based on the distribution of clusters younger than 700 Myr, we found a Solar offset of $z_\odot = -17.0 \pm 0.9 \text{ pc}$, and estimated the scale height $z_h = 91.7 \pm 1.9 \text{ pc}$ from the Galactic plane and $89.6 \pm 2.6 \text{ pc}$ from the reddening plane. The interstellar extinction is found varying in a sinusoidal manner with the Galactic longitude and maximum and minimum Galactic absorption occurring in the longitudinal direction of $59^\circ \pm 10^\circ$ and $239^\circ \pm 10^\circ$, respectively.

Conclusions. Having a large catalogue of open clusters with different physical parameters, the Galactic disk morphology in the extended Solar neighbourhood is untangled. This study allows us to investigate the properties of the Galactic disk, spiral arms, and reddening distributions and we could reveal a layer of interstellar material with varying thickness along the Galactic longitude that is inclined with respect to the formal Galactic plane.

Key words. Open clusters: general; Galaxy: structure, spiral arms; extinction – interstellar matter; method: statistical

1. Introduction

Star clusters are excellent tracers to probe the evolution of the Galaxy. As open clusters (OCs) are relatively younger populations and mostly lie within the Galactic disk, these sources are being viewed as excellent markers to study the structural, kinematical, and chemical properties of the Galactic disk through analysis of the largest possible number of clusters in the Galaxy. Such studies have been carried out by many authors in the past (cf., Bonatto et al. 2006; Buckner & Froebrich 2014; Joshi et al. 2016; Cantat-Gaudin et al. 2020; Dobbs et al. 2022). In recent years, the number of OCs has grown multi-fold paving a way for a better understanding of the Galactic disk, thanks to large-scale surveys and machine-learning methods (Cantat-Gaudin et al. 2018; Ryu & Lee 2018; Sim et al. 2019; Cantat-Gaudin et al. 2019; Liu & Pang 2019; Dias et al. 2021; He et al. 2021; Hao et al. 2022; Castro-Ginard et al. 2022). The accurate physical parameters for OCs are obtained through analysis of precise membership identification of cluster stars facilitated through their kinematic parameters (Dias et al. 2014; Cantat-Gaudin et al. 2018; Dias et al. 2021; Castro-Ginard et al. 2022; Zhong et al. 2022). This consequently offers a great opportunity

to detect many new cluster members hence increasing the cluster sample in the Milky Way (cf., Cantat-Gaudin et al. 2018; Castro-Ginard et al. 2022). It is important to note that much of this progress has come from Gaia survey data which provide unprecedented homogeneous and precise photometry, high-precision proper motion, and parallaxes of more than a billion sources (Gaia Collaboration et al. 2016, 2018).

The interstellar extinction acts as a tracer of the interstellar material, an important component of the Galactic disk. The distribution of interstellar reddening material in the Galaxy is widely perceived as an excellent means to probe the Galactic disk structure and infer various parameters like scale height and Solar offset. Several studies have been undertaken in the past to strengthen our knowledge of the distribution of the interstellar extinction in our Galaxy (Pandey & Mahra 1987; Chen et al. 1998; Joshi 2005; Sharma et al. 2007; Chen et al. 2014; Guo et al. 2021) and refine above parameters. In the last few years, reddening information has become available for a few thousand OCs. With the continuous increase in the data sample and more reliable physical parameters obtained through Gaia survey data, it is imperative to re-investigate the Galactic disk, spiral arms, and distribution of reddening material in the Galactic plane with an improved set of cluster parameters and reddening information to understand the Galactic disk morphology in the solar neighbourhood.

* E-mail: yogesh@aries.res.in

** Data used in the present study is only available in the electronic form at the CDS via anonymous ftp to cdsarc.u-strasbg.fr

This paper is organized as follows: we describe the data used in the present study in Section 2. The spatial distribution of the clusters in the Galaxy is described in Section 3. In Section 4, we discuss the OC distribution along and perpendicular to the Galactic plane. The study of extinction in the Galactic disk is carried out in Section 5. The summary of our results is laid out in Section 6.

2. Data

This catalogue is compiled using several previous studies on OCs providing the mean astrometric and physical parameters of the OCs. Since there have been some studies in recent times (e.g.; [Cantat-Gaudin & Anders 2020](#)) indicating that many OCs detected before the release of Gaia survey data may be false positives, we only considered the OCs detected in the Gaia era. While prioritizing the latest studies and giving lesser weight to those showing multiple discrepancies, we compiled a catalogue of 6133 OCs having information about positions, parallax, age, heliocentric distance, proper motions, radial velocities, color excess, and extinction, though not all the parameters are available for all the clusters. We preferred the cluster parameters from post-Gaia catalogs and only resorted to the pre-Gaia studies if no information was found in recent studies. Of the 6133 OCs, only 4378 clusters have distance and age information which we consider in the subsequent analysis except otherwise stated. Among them, 2959 OCs have distance estimates from the Gaia data while the remaining 1419 OCs have distances retrieved from pre-Gaia era studies which might contain higher uncertainties. Using the distance information, we estimated (X, Y, Z) cartesian coordinates as well as galactocentric distance R_{GC} for all the 4378 OCs.

To investigate the distribution of interstellar reddening material in the solar neighbourhood, we converted the total extinction A_V in the V band to the selective extinction $E(B - V)$ using the value of their ratio, that is total-to-selective extinction $R_V = \frac{A_V}{E(B-V)}$, whose average value is observationally found to be 3.1 for the normal dust-to-gas ratio. While compiling the cat-

alog, we found there were many OCs for which we had contradicting values of the total extinction A_V and the selective extinction $E(B - V)$ in the sense that their ratio was way off from the typical value of 3.1. More so, there were clusters for which the value of $E(B - V)$ reported in a pre-Gaia catalogue was higher than A_V reported for the same clusters in the post-Gaia catalogs. To remove such discrepant clusters we only considered OCs having $R_V = 3.1$ with a tolerance limit of 33% (or ± 1.0) ([Cambr sy et al. 2005](#)) due to variation in the normal dust-to-gas ratio among different regions while rejecting other clusters. We found 1254 such clusters for which the values of both $E(B - V)$ and A_V were available in the catalog. Among them, 448 clusters had discrepant color excess and extinction values that did not agree with each other within the tolerance limit. For the rest of the clusters, we prioritized the post-Gaia studies while compiling for the reddening of OCs. Finally, we transformed the total extinction A_V to $E(B - V)$ by dividing R_V . Figure 1 shows the distribution of OCs in the $A_V - E(B - V)$ plane. The blue (top), orange (middle) and red (bottom) lines depict the slope of 4.1, 3.1, and 2.1 respectively. The black dots represent the OCs included in the catalogue whereas the OCs depicted by gray dots were rejected from further analysis. In total, we extracted 4233 OCs for which the extinction parameter has been considered in the present study. Of these, there were 3787 OCs having both reddening as well as distance information along with their age estimates.

3. Spatial distribution

3.1. 2D distribution of OCs and present-day Spiral Arms

The knowledge of the spatial distribution of OCs is important to understand the inhomogeneous nature of the Galaxy and probing the large-scale Galactic structure. For this purpose, we use the positional coordinate of all the 6133 OCs to infer the broader picture of the structure of the Milky Way. In Figure 2, we show an on-sky view of the Galaxy in the Galactic longitude-latitude ($l - b$) plane where clusters are juxtaposed in the $l - b$ plane. It is evident that there are few pockets where cluster density is low like 50° and 150° Galactic longitude regions. The lack of OCs in a region near $l \sim 150^\circ$ might be due to the lower density of gas and dust in the anti-center direction and has also been noticed earlier and dubbed as Gulf of Camelopardalis ([Cantat-Gaudin et al. 2019](#); [Castro-Ginard et al. 2019](#)). The deficiency of clusters around $l \sim 50^\circ$ region is mainly caused by the higher disruption rate complemented by our obscured view in the direction of the Galactic centre. The distribution of clusters is more scattered around the Galactic mid-plane towards the Galactic anti-center direction than in the direction of the Galactic center. However, in general, most of the clusters are confined very close to the Galactic mid-plane and number density sharply decreases as one goes away from the mid-plane with more than 85% of the total number of OCs belonging to $[-10^\circ, 10^\circ]$ of the Galactic latitude while 75% of them belong to central $[-5^\circ, 5^\circ]$ region.

To better resolve the multiple structures at various distances which are otherwise superposed on the sky, we illustrated the $X - Y$ distribution of OCs in the left panel of Figure 3 having the Sun at $(-8.15, 0)$ kpc ([Reid et al. 2019](#)) and Galactic center at the origin. Here, we draw only 4378 OCs for which distance information is available. The OCs detected very far away from the Galactic center are not shown in this plot for better visualization. The OCs older than 700 Myr are shown in gray color while the younger ones are colored according to their ages. The position of the OCs shown in Figure 3 reveals the spiral structure of

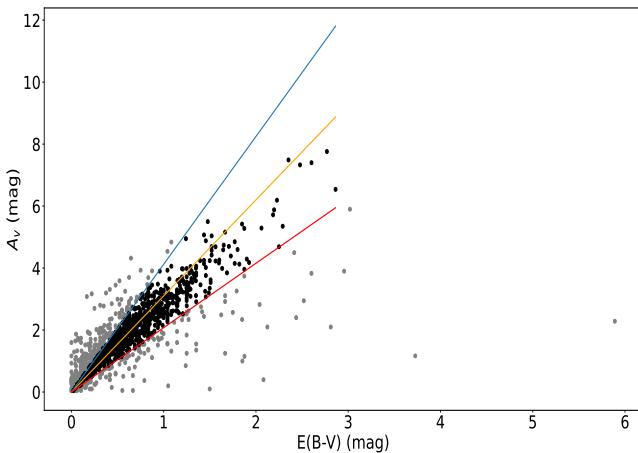


Figure 1: Comparison of A_V and $E(B - V)$ for a sample of 1254 OCs that have both A_V and $E(B - V)$ values in the catalog. The lines denote a slope of 4.1, 3.1, and 2.1 from top to bottom respectively and the OCs satisfying the condition mentioned in the text are denoted by black dots enclosed within the blue (top) and the red (bottom) lines. The gray dots represent the OCs for which the A_V and $E(B - V)$ values were found to be discrepant.

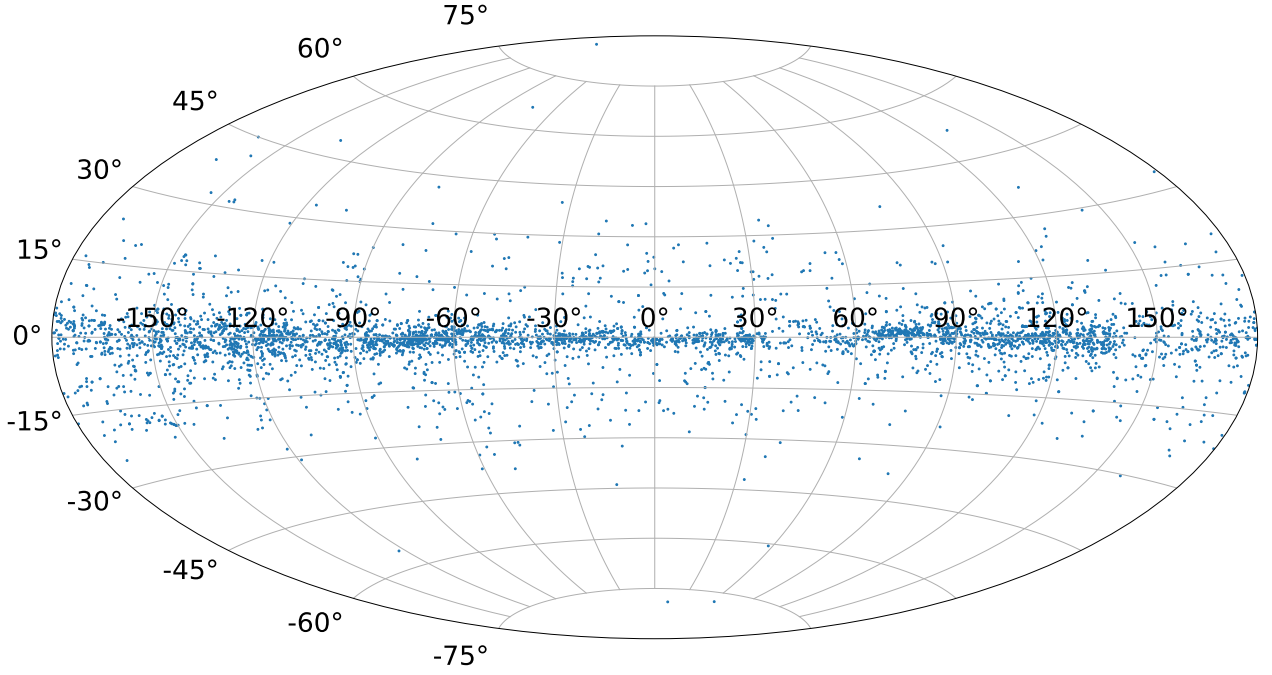


Figure 2: An on-sky view of Galaxy in the Galactic longitude-latitude ($l - b$) plane juxtaposed with our sample of 6133 OCs.

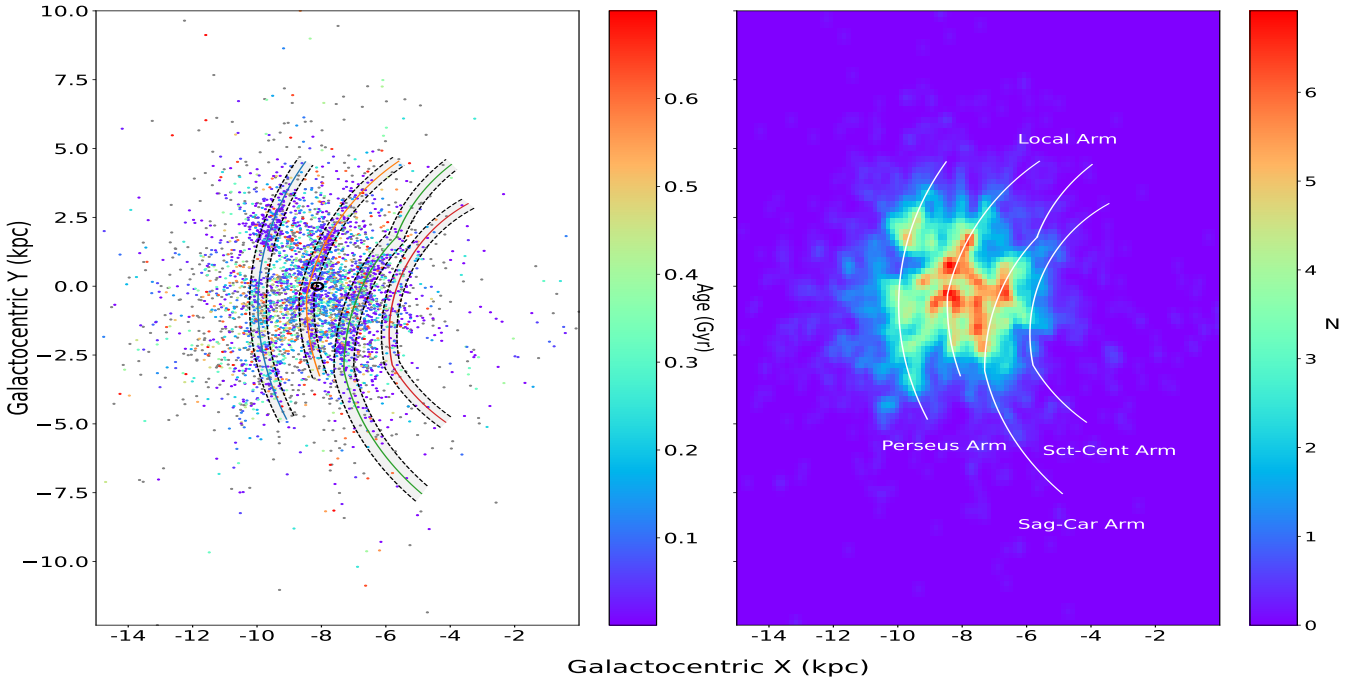


Figure 3: Distribution of the complete sample of OCs in the $X - Y$ plane with the Galactic center at the origin. OCs younger than 700 Myr are color-coded based on their age while the older ones are shown in gray color. The position of the Sun is marked with a black circle at $(-8.15, 0)$ kpc. The right panel of the figure shows the density heat map for the same sample. Spiral Arms are taken from Hou (2021).

the Galaxy as shown by the usual log-periodic spiral arms taken from Hou (2021) where the profile of each arm is described by Reid et al. (2019) as following

$$\ln(R/R_{kink}) = -(\beta - \beta_{kink}) \tan \psi$$

where R is the Galactic radius at a galactocentric azimuth angle β which is 0 along the line joining the Sun and the Galactic

center and increases in the direction of Galactic rotation. R_{kink} and β_{kink} are the corresponding values of R and β at the kink position, where there might be an abrupt change in the pitch angle ψ . Hou (2021) models each of the spiral arms with one kink except the Sagittarius-Carina Arm which is described using two kinks at $\beta = -22.8^\circ$ and 17.5° , respectively. The regions enclosed within the dashed lines around the spiral arms correspond

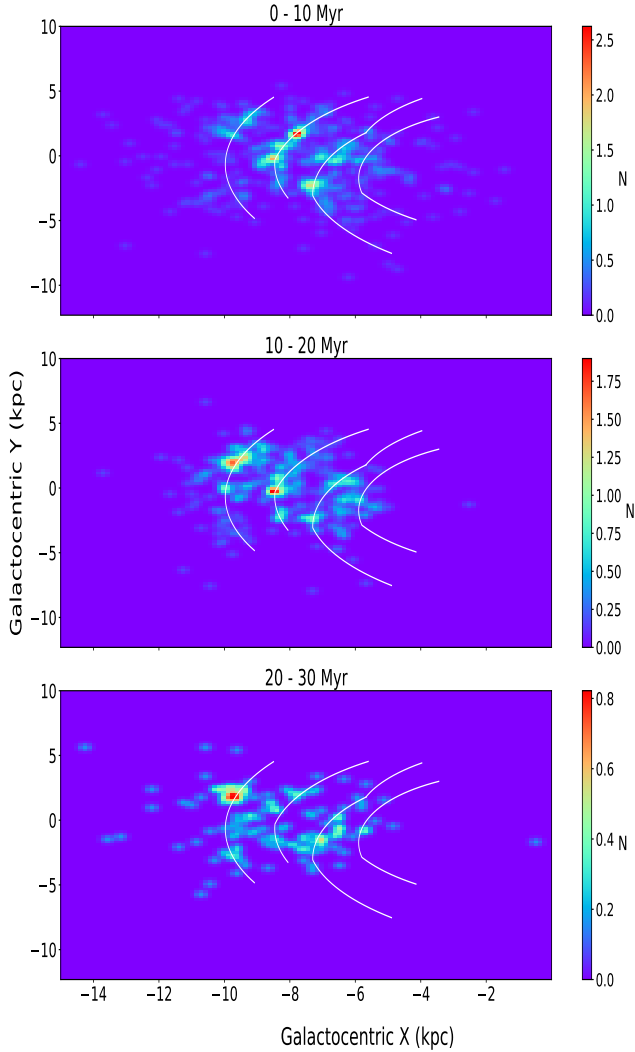


Figure 4: Same as the right panel of Figure 3 but for different age intervals of ≤ 10 Myr, 10 - 20 Myr, and 20 - 30 Myr from top to bottom. Spiral arms are traced by the OCs younger than 10 Myr and the older ones occupy the inter-arm regions. Further, the spiral structure loses its shape in the 20 - 30 Myr age range.

to the arm widths. The distribution of OCs in spiral arms is not uniform but shows a patchy appearance. It is observed that the spiral arms are populated by younger clusters while older clusters are mainly present in the inter-arm regions as has also been reported in previous studies by Cantat-Gaudin & Anders (2020); Monteiro et al. (2021); Hou (2021); Tarricq et al. (2021), and Poggio et al. (2021).

The density heat map of the OCs is also drawn in the right panel of Figure 3 which helps us in understanding a general trend of the distribution of OCs in the spiral arms. One can see a large number of OCs fill both spiral arms and inter-arm regions. The density heat map shows a high density of OCs in the Local arm and Sagittarius-Carina arm, and only a few of them are populated in Perseus and Scutum-Centaurus arms. The Perseus arm gap in the direction of the Galactic anti-center is also evident in the density heat map as has also been observed by Poggio et al. (2021) and Sakai et al. (2022). The high density is also seen in the inter-arm region between the Local and the Sagittarius-Carina Arm. It is believed that the Local Arm is an arm branch located between the Perseus and the Sagittarius-Carina Arm (e.g., Hou 2021). As

expected, we see many OCs in the Local Arm due to the high observation rate of OCs in the solar neighbourhood.

In Figure 4, we plot the same distribution for three different samples of OCs based on their ages viz., (i) $Age/Myr \leq 10$ (top panel), (ii) $10 < Age/Myr \leq 20$ (middle panel), and (iii) $20 < Age/Myr \leq 30$ (bottom panel). This displays the respective locations of 501, 355, and 141 OCs in the $X - Y$ plane. The demarcation of clusters in terms of age band is crucial for untangling the spiral arm structure as it has been known for a long time that young OCs are ideal tracers of the Galactic spiral arms. The plots depict spiral arms defined by Hou (2021) overplotted as curved solid lines in each of the subplots of Figure 4. The importance of one or more kinks, as also proposed by Reid et al. (2019) and Hou (2021), in the spiral arms becomes clear in the top panel of the Figure 4, especially in the case of the Local and Sagittarius-Carina Arms. One can observe that the younger OCs ($Age < 10$ Myr) clearly trace out the spiral arms in the solar neighbourhood and occupy the inter spiral arm regions as they age while most of the OCs having their age in the range 20-30 Myr are well off from the spiral arms. This means that, in general, most of the OCs leave their birth site after about 10 to 20 Myr and start populating in the inter-arm regions where they stay for the rest of their life. Castro-Ginard et al. (2021) has also noted, however with different age bins, that the OC overdensities showed increased dispersion with time. Moreover, it was also observed that a large number of clusters do not survive longer than 10-15 Myr after their birth with the death rate decreasing progressively as they become older and leave the spiral arms (Monteiro et al. 2021).

3.2. Spiral Pattern rotation speed

The determination of spiral pattern rotation speeds can provide us with key insights into the nature and evolution of spiral arms. Since the parameters of OCs can be determined with high precision by averaging over the members, one can make use of their kinematic data to estimate the pattern speed of spiral arms (Dias & Lépine 2005; Gerhard 2011). Some recent studies on the determination of spiral pattern rotation speeds include Castro-Ginard et al. (2021) which have made use of 264 young OCs while Griv et al. (2022) analysed 252 OCs within 3 kpc of the Sun and having age < 100 Myr. Taking advantage of a large number of OCs available in the present study, we re-investigated the rotation speeds of spiral arms in the following analysis.

Before, proceeding further, we needed to identify the host arms for the OCs. This was done by the arm assignments of the OCs lying within 0.4 kpc of their nearest arm. Figure 5 shows each arm and the corresponding OCs in the $\log(R) - \beta$ plane, where R and β are the same as defined in the previous section. The arm assignment was unambiguous in most of the cases and was supplemented with the kinematic data of OCs in the case of clusters near the borders. We also included the OCs which were not in the β range of present-day spiral arms but were part of their appropriate extensions as seen in the case of the Local and the Perseus Arms in the figure. We have taken the solar distance from the Galactic center R_{\odot} as 8.15 kpc and the circular rotation speed at the solar position $\Theta_0 = 236 \pm 7$ km s^{-1} Reid et al. (2019). We restricted the OCs age within ≤ 80 Myr that yielded us a total sample of 444 OCs having 110, 178, 116, and 40 OCs in Perseus, Local, Sagittarius-Carina (Sag-Car), and Scutum-Centaurus (Sct-Cent) arms, respectively which also have the information available for their radial velocities. Figure 6 shows the age distribution of OCs in each arm where we observe a gradual decline in the number of OCs as the age increases. This

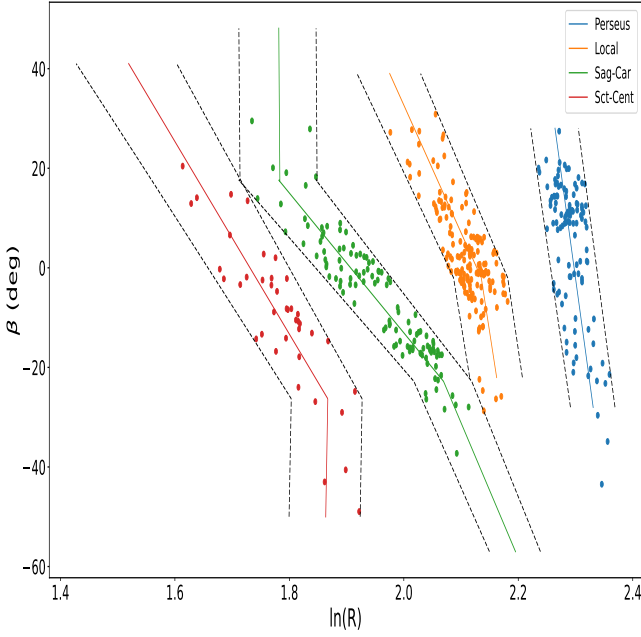


Figure 5: Distribution of OCs in $\log(R) - \beta$ plane after arm assignments. The solid lines denote the spiral arms taken from Hou (2021) whereas the dashed lines indicate a width of 0.4 kpc for each spiral arm.

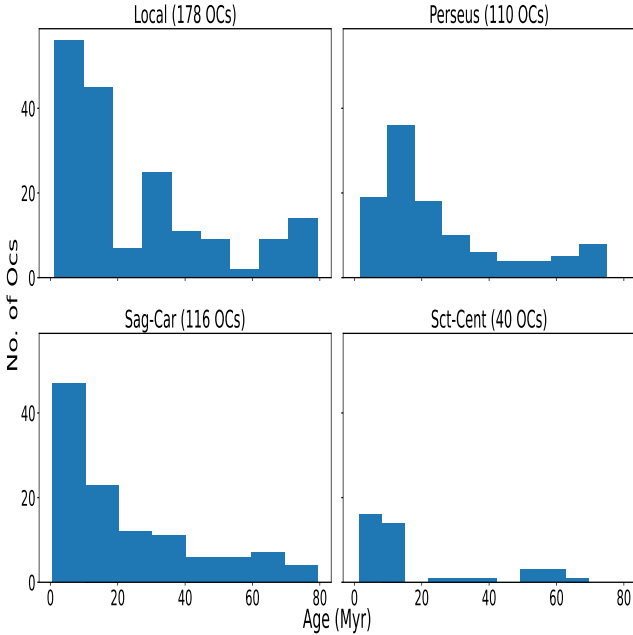


Figure 6: Age distribution of OCs belonging to each spiral arm. The number of clusters assigned to each arm is mentioned in parentheses. As expected the counts of observed clusters decrease as the age increases.

might be caused due to two factors, (i) the older OCs might have undergone disruption due to close encounters with other clusters and clouds of gases, (ii) the OCs would have migrated away from the spiral arms both in radial and vertical directions and might no longer be close enough to be considered as a part of the spiral arms (Chen & Zhao 2020; Zhang et al. 2021).

Table 1: Spiral Arm rotation speeds for different age intervals

Arm	No. of OCs	Ω_{rot}		
		(10 - 80 Myr)	(10 - 50 Myr)	(50 - 80 Myr)
Perseus	110	24.64 ± 0.5	24.13 ± 0.88	26.82 ± 3.5
Local	178	26.42 ± 1.29	26.48 ± 1.43	26.44 ± 1.44
Sag-Car	116	26.09 ± 0.51	26.14 ± 0.38	25.74 ± 1.44
Sct-Cent	40	28.85 ± 2.69	29.55 ± 2.86	–

Since OCs younger than 10 Myr trace the Milky Way spiral arms quite well and only begin to move away at an age of about 10 to 20 Myr, we used the OCs older than 10 Myr to estimate the rotational speed of the spiral arms. We adopted a similar methodology proposed by Dias & Lépine (2005) to compute the pattern speed Ω corresponding to each arm:

- Arm assignment was done for each OC and each arm was studied separately.
- Birthplaces were found by integrating the orbit of each OC backward and it was assumed that these birthplaces represent points on the spiral arm time T ago where T denotes the age of each cluster.
- Once we had the birthplaces of OCs, we assumed that the spiral arms traverse a circular path in the Galactic $X - Y$ plane with time and calculated the present-day Galactic azimuths for a particular pattern speed Ω given the Galactic azimuths corresponding to the birthplaces of OCs. Mathematically,

$$\beta_{G,present} = \beta_{G,birth} + \Omega \cdot T$$

- We estimated the optimal value of Ω by minimising the distance between the present-day spiral arms and their integrated present-day locations.

We performed the OC orbit integration following the MWPotential2014 of the Python package GALPY (Bovy 2015) which is fit to various observational constraints and is composed of a spherical nucleus and a bulge, Navarro-Frenk-White dark matter halo and a Miyamoto-Nagai disc. The numerical integration was done using the Leapfrog integration scheme where the orbits were traced back in steps of 0.1 Myr. Also, we have rejected the data points on the integrated spiral arms that did not lie within 0.4 kpc of the analytical spiral arms wherein the number of rejected data points varies on using different values for Ω . Since uncertainty in age is the dominant source of error in the computed birthplaces, we estimated the typical value of the error in age, whenever available, to be about 20% which is close to the value of 22% average age error for a sample of 581 OCs reported by de la Fuente Marcos & de la Fuente Marcos (2004). Hence, we iterated the above process 100 times by using the age values of clusters with corresponding random errors ranging from 0 - 20%. The mean value and the standard deviation are reported in Table 1 as the optimal and the corresponding dispersion in the pattern speed Ω .

We also computed the pattern speeds of each spiral arm for different age bins to investigate if the spiral arms have accelerated in the last 80 Myrs. The resultant values are given in Table 1. The optimal value of Ω for the Scutum-Centaurus arm could not be determined for the 50 - 80 Myr age interval due to very few OCs lying in the bin (7 OCs) as is evident from the Figure 6. It can be seen that the values of Ω obtained for each arm corresponding to a particular age bin agree well within the errors showing that the arms rotate as a rigid body with the same angular velocity Ω , hence supporting the density wave theory. Also, comparing the values of pattern speed across different age intervals, we can infer that the arms have not accelerated in the last ~

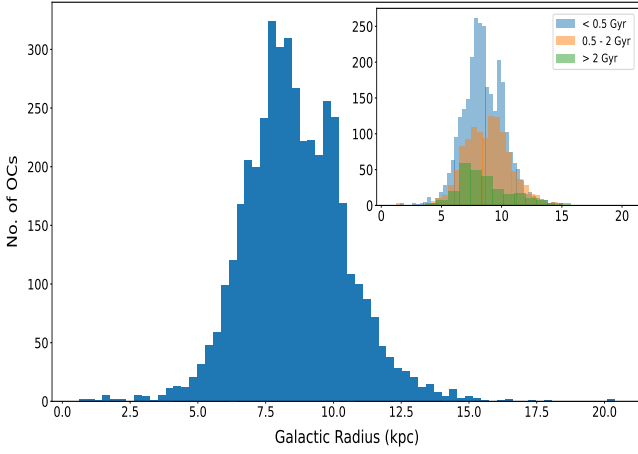


Figure 7: Number distribution of OCs as a function of the Galactic radius. The inset shows the same distribution but for different age intervals viz, < 0.5 Gyr, $0.5 - 2$ Gyr, and > 2 Gyr. A dip in the counts is observed at ~ 9 kpc in the distribution for the full sample and the young OCs. This dip loses its significance in the case of older OCs (Age > 500 Myr) which suggests the radial migration of OCs with time.

80 Myrs. Dias & Lépine (2005), Dias et al. (2019) and Monteiro et al. (2021) obtained a similar conclusion using a sample of dozens of OCs. However, we could not compare the exact values of the pattern speed among different studies due to the difference in the values used for the solar radius R_{\odot} and circular rotation speed at solar position V_{\odot} . The results of Castro-Ginard et al. (2021) on the other hand, contradict the classical density wave theory and support the model of flocculent spirals or tidally induced arms for the Milky Way as they show that the pattern speeds of the spiral arms fall closely with the Galactic rotation curve as one moves farther away from the Galactic center. The analysis of our sample of 444 OCs, the largest sample of OCs used for the study of the determination of spiral pattern speed of the Galaxy, supports the rigid body rotation of the spiral arms with an Ω of $26.5 \pm 1.5 \text{ km s}^{-1} \text{ kpc}^{-1}$ which has been constant in time for at least the last ~ 80 Myr.

3.3. 9 kpc gap and derivation of corotation radius

Figure 7 illustrates the distribution of our cluster sample as a function of the projected Galactocentric distance with the inset depicting the same distribution but for three different age intervals of < 0.5 Gyr, $0.5 - 2$ Gyr and > 2 Gyr. A similar distribution was also studied by Monteiro et al. (2021) but for a smaller sample of 1750 OCs. Both studies show a dip in the number of detected clusters at about 9 kpc from the Galactic center, especially in the case of younger OCs. One can see that the gap disappears for older OCs hence suggesting the radial migration of OCs with the age. A similar gap has been observed in previous studies using other Galactic tracers by Amôres et al. (2009) and Barros et al. (2013).

Once we determined Ω , we could further calculate the corotation radius (R_c) such that $R_c = \frac{V_{rot}(R_c)}{\Omega}$ where V_{rot} is the velocity obtained from the Milky Way rotation curve which we calculated using the MWPotential2014 through GALPY (Bovy 2015). The values R_{\odot} and V_{\odot} used to normalise the rotation curve are the same as adopted in previous sections. We obtained the value of corotation radius R_c as $8.83^{+0.48}_{-0.46}$ kpc i.e $R_c = 1.08^{+0.06}_{-0.05} R_{\odot}$ which

is very close to the solar orbit. This coincides with the observed gap in the number distribution of OCs at ~ 9 kpc in Figure 7. Monteiro et al. (2021) explains this gap using the corotation radius and argues that the corotation leads to a division of the Galaxy into two parts viz, internal and external to the corotation radius each of which possesses different properties as they evolve with time. In the Figure 8 of Monteiro et al. (2021), they provide a schematic representation of the flow of gas near the corotation radius and show how the opposite flow directions on the two sides of this radial distance lead to a minimum in the gas density near 9 kpc resulting in inhibited star formation at that point, thereby leading one to observe a fewer number of OCs in that region. This also prevents the mixing of gas on the two sides of the corotation radius thus favoring an independent chemical evolution on both sides of the solar orbit.

4. Distribution of OCs perpendicular to the Galactic plane

It is known that the number density of the OCs is maximum near the Galactic plane and falls steadily as one goes away from the mid-plane ($b = 0^\circ$). In Figure 8 (a), which shows the vertical distance distribution ($z = d \sin b$), we divided the cluster sample into different bins in z with a bin-width of 20 pc, wherein the number distribution peaks at $z \sim -15$ pc. Since there were very few OCs at larger vertical distances, we have restricted z for OCs within 2 kpc from the Galactic plane, up to which OCs sample is found to be complete. This has left us with 4372 OCs which are used in the following analysis.

4.1. Solar offset

It is normally assumed that the cluster density distribution perpendicular to the Galactic plane can be well described in the form of a decaying exponential away from the Galactic plane, as given by Chen et al. (1998),

$$N = N_0 \exp \left[- \frac{|z + z_{\odot}|}{z_h} \right] \quad (1)$$

where z_{\odot} and z_h are the solar offset and scale height, respectively. The knowledge of the exact value of z_{\odot} is important not just for the Galactic structure models but also in describing the north-south asymmetry in the density distribution of different kinds of stellar populations in the north and south Galactic regions (Cohen 1995; Chen et al. 1999). However, to accurately determine the solar offset, we need to consider the OCs close to the Galactic plane to prevent any bias induced by very far away clusters. To do this we applied the age cut-off for OCs as the clusters start drifting away from the Galactic mid-plane as they age. We refer the reader to Figure 2 of Joshi (2007) and on using the same methodology, we only considered the OCs younger than ~ 700 Myr. We determined z_{\odot} by fitting the above exponential function to the sample of OCs younger than 700 Myr and obtained an estimate of $z_{\odot} = -17.0 \pm 0.9$ pc. Numerous studies have estimated z_{\odot} using a wide variety of celestial sources and most of these studies obtained z_{\odot} in the range of 10 to 25 pc in the north direction of Galactic plane (e.g., Joshi 2007; Majaess et al. 2009; Buckner & Froebrich 2014; Yao et al. 2017; Siebert 2019; Cantat-Gaudin et al. 2020) with a median value of around -17 ± 2 kpc (Karim & Mamajek 2017). Though it is found that the choice of the data sample and method of determination account for most of the disagreements among z_{\odot} values (Joshi 2007; Cantat-Gaudin et al. 2020), however, our present estimate is in remarkable agreement with Karim & Mamajek (2017) median solar offset value.

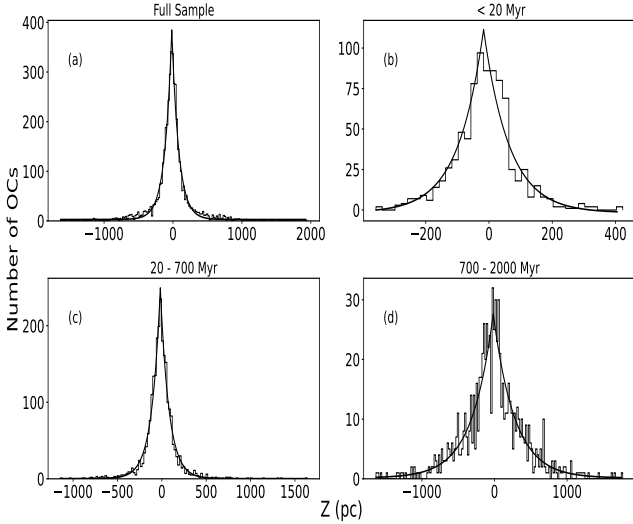


Figure 8: Z distribution of OCs corresponding to different age intervals. The scale height is estimated while assuming a constant solar offset z_{\odot} of -17.0 ± 0.9 pc for all the plots. The sample is restricted to $(-2, 2)$ kpc in z and the best fit for exponential decay is shown by a continuous line.

4.2. Cluster scale height

The observed clusters distribution perpendicular to the Galactic plane provides us with an estimate of the thickness of the young Galactic disk. We fitted the number distribution of OCs in the exponential profile as described in Eq. (1) to estimate the scale height. The resulting best fit is illustrated in Figure 8 (a) for the sample of 4378 OCs. The scale height of the distribution of clusters is found to be $z_h = 100.8 \pm 1.7$ pc. However, the large value of z_h is mainly influenced by the older clusters which are mainly located at higher latitudes resulting in a shallower wing in the z distribution. We plot the similar distribution of OCs perpendicular to the Galactic plane but using different age bins viz., < 20 Myr, $20 - 700$ Myr, $700 - 2000$ Myr corresponding to 837, 2439, and 831 OCs respectively wherein the majority of the sample is dominated by the intermediate age OCs. We fitted the exponential profile in all these three samples to estimate the scale height, while keeping the solar offset $z_{\odot} = -17.0$ pc as a fixed value as derived in the previous section. The resulting best fit is illustrated in Figure 8(b,c,d). In addition, we also determined scale heights for the larger cluster sample having age < 700 Myr, and < 2000 Myr. Table 2 provides information about the scale heights obtained for different age bins and the corresponding number of OCs. The scale height increases as we fit the exponential distribution to older OCs, which is consistent with the hypothesis that OCs migrate toward the outer disk as they age. For a sample of OCs younger than 700 Myr, z_h is obtained as 91.7 ± 1.9 pc. A range of cluster scale heights has been published by authors in previous studies. For example, Bonatto et al. (2006) derived a scale height of 48 ± 3 pc for OCs younger than 200 Myr; Joshi et al. (2016) obtained $z_h = 64 \pm 2$ pc for OCs within 1.8 kpc of the Sun. Buckner & Froebrich (2014) found the scale height increases from about 40 pc at 1 Myr to 75 pc at an age of 1 Gyr. Some more recent studies such as Cantat-Gaudin et al. (2020) obtained a scale height of 74 ± 5 pc for OCs in the solar neighbourhood with a typical age of ~ 100 Myr. Similarly, Hao et al. (2021) reported a scale height of 70.5 ± 2.3 pc for young OCs (Age < 20 Myr) which increases to 87.4 ± 3.6 pc for older OCs

Table 2: Estimated scale heights for different age intervals while keeping the solar offset $Z_{\odot} = -17.0 \pm 0.9$ pc fixed.

Age Interval (Myr)	Z_h (pc)	No. of OCs
Full Sample	100.8 ± 1.7	4372
< 20	80.8 ± 8.0	837
< 700	91.7 ± 1.9	3376
< 2000	98.8 ± 1.6	4107
$20 - 700$	96.4 ± 1.9	2439
$700 - 2000$	294.7 ± 19.5	831

with ages of $20 - 100$ Myr. Although it is difficult to compare different estimates due to their different sample selection criteria but our present value of $z_h = 91.7 \pm 1.9$ pc for clusters younger than < 700 Myr, is well in agreement with most of these recent estimates.

Further, it has also been established that the OCs farther away from the Galactic center are present at higher altitudes from the Galactic plane hence resulting in the variation of z scale height as a function of the projected Galactocentric distance (R_{GC}). Bonatto et al. (2006) observed that the scale height increases by a factor of two when one compares the two estimates for OCs inside and outside the solar circle. Buckner & Froebrich (2014) and Joshi et al. (2016) showed a positive trend between the galactocentric distance and the scale height. Using our OC sample, we calculated the scale height (z_h) for two cases (i) $R_{GC} \leq 8.15$ kpc (ii) $R_{GC} > 8.15$ kpc comprised of 1865 and 2513 OCs respectively. Here, 8.15 kpc is taken as the location of solar orbit (Reid et al. 2019). We obtained z_h to be 79.2 ± 1.6 pc and 138.1 ± 1.7 pc for the two cases respectively, which further affirms dependence of z_h on the Galactocentric distance, in agreement with both these studies.

5. Galactic reddening distribution

The study of the distribution of interstellar extinction, A_V , is important for many investigations of Galactic and extragalactic sources (Pandey & Mahra 1987; Chen et al. 1998; Joshi 2005). However, the patchy distribution of dust and gas within the Galactic disc makes it difficult to obtain the precise determination of the A_V values for most of the OCs. The present data sample, about 3800 clusters have both A_V and distance information which allows us to study the Galactic reddening distribution in the solar neighbourhood. In the following analysis, we examine the spatial distribution of interstellar extinction in the solar neighbourhood and investigate the Galactic plane defined by the reddening material, which is normally known as the reddening plane.

In Figure 9 we show the heat map of the distribution of reddening material in the $l - b$ plane where the colors signify the amount of reddening present in the cluster positions. As expected, the reddening material is highly concentrated in the Galactic mid-plane and decreases with the increasing Galactic latitude. About 90% of the reddening material is found to be located within $|b| = 10^\circ$. On the other hand, there are 3272 OCs ($\sim 85\%$) within $|b| \leq 10^\circ$ in our cluster sample. Because of the thinness of the reddening distribution around the Galactic mid-plane where a majority of the interstellar material lie, it is imperative to examine the dust distribution close to the mid-plane therefore we restrict ourselves to the OC sample to within $|b| \leq 10^\circ$ that is used in the following analysis.

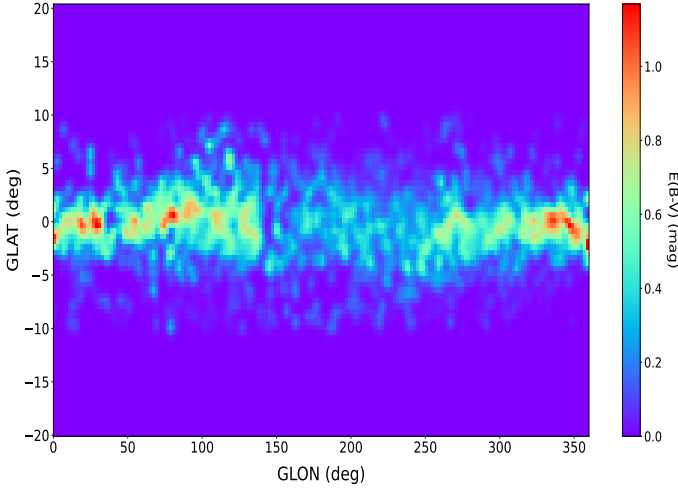


Figure 9: Heat map of the distribution of reddening material in the $l - b$ plane. The colors in the heat map represent the mean reddening of the cluster.

5.1. Reddening distribution perpendicular to the Galactic plane

To understand the reddening distribution perpendicular to the Galactic plane, we draw the mean reddening in the direction of OCs as a function of their mean absolute vertical distance z in Figure 10. The bin width in z is set to be 50 pc. The resulting distribution is fitted with a straight line shown by a continuous line in the same figure. The least-square fit in mean $|z| - E(B - V)$ gives following equation

$$\overline{E(B - V)} = -0.35 * \overline{|z|} + 0.66$$

$$\pm 0.04 \quad \pm 0.01$$

However, when we draw independent linear fit above and below the Galactic plane in the mean reddening with respect to mean absolute vertical distance, we obtained two very similar equations as the following,

$$\overline{E(B - V)} = -0.33 * \bar{z} + 0.67 \quad (z \geq 0)$$

$$\pm 0.03 \quad \pm 0.02$$

$$\overline{E(B - V)} = -0.34 * \bar{z} + 0.64 \quad (z < 0)$$

$$\pm 0.04 \quad \pm 0.02$$

for the rising and falling branches around the mean value. This shows that the reddening varies in a similar manner along the north and south directions of the Galactic mid-plane with a typical slope of $-0.35 \pm 0.04 \text{ mag pc}^{-1}$ though reddening does not seem to vary much beyond 1 kpc in the z -plane. A negative slope in $\frac{dE(B-V)}{dz}$ means a lesser amount of absorbing material is present as we go away from the Galactic mid-plane in the perpendicular direction where relatively older clusters are located devoid of dust and gas in their surrounding. In our earlier study based on the reddening information for 1211 OCs within 1.8 kpc of the Sun, we found this slope as $0.41 \pm 0.05 \text{ mag pc}^{-1}$ (Joshi et al. 2016) thus our present estimate is slightly smaller than the earlier reported value but consistent within the quoted error.

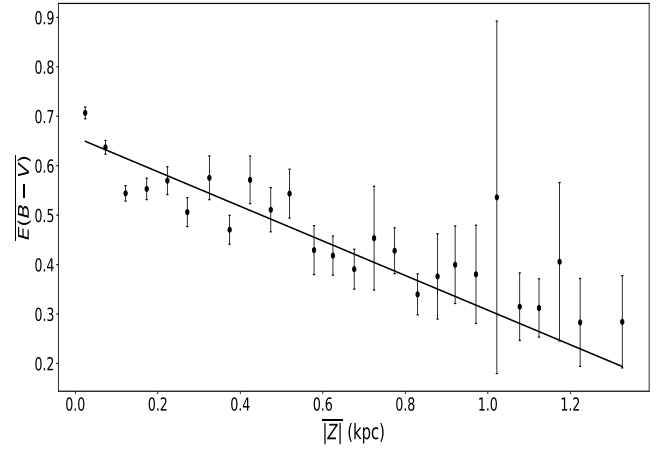


Figure 10: Mean value of $E(B - V)$ as a function of mean $|z|$ for the same data sample. The least squares fit shown by a continuous line.

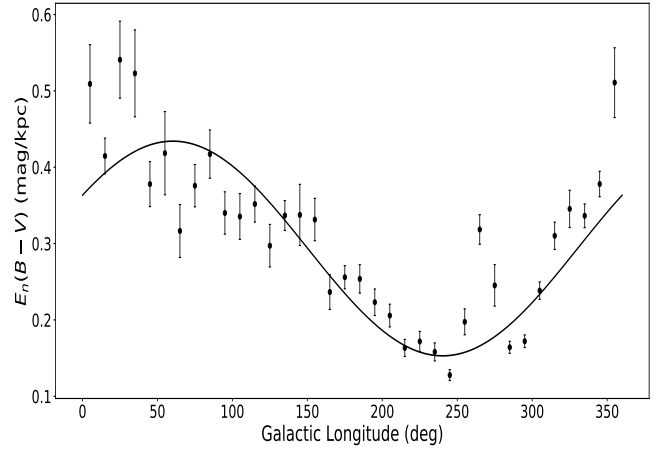


Figure 11: Mean normalised reddening as a function of Galactic longitude in bins of 10° along with the sinusoidal fit depicted by a continuous line.

5.2. Galactic absorption

To study the Galactic absorption in the sky, we normalized the cluster extinction by its distance

$$E_n(B - V) = \frac{E(B - V)}{d}$$

where d is the distance of the cluster from the Sun. We plot the variation of mean Galactic absorption in bins of 10° Galactic longitude in Figure 11. The amount of mean Galactic absorption shows more scatter in the direction of the Galactic center while less scatter and more systematic variations are seen towards the anti-center direction of the Galaxy. Though the clusters have a range of reddening values for the same Galactic longitude, a lesser absorption is seen in the region of $l \sim 240^\circ$ while the clusters in the region of $l \sim 50^\circ$ are found to possess higher absorption. The low and high extinction in certain directions is indicative of the varying amount of interstellar material present in those directions. When we fit a best fit sinusoidal in Figure 11, we found an equation of the following form

$$E_n(B - V) = 0.29 + 0.14 \sin(l + 29.8)$$

$$\pm 0.01 \quad \pm 0.01 \quad \pm 4.6$$

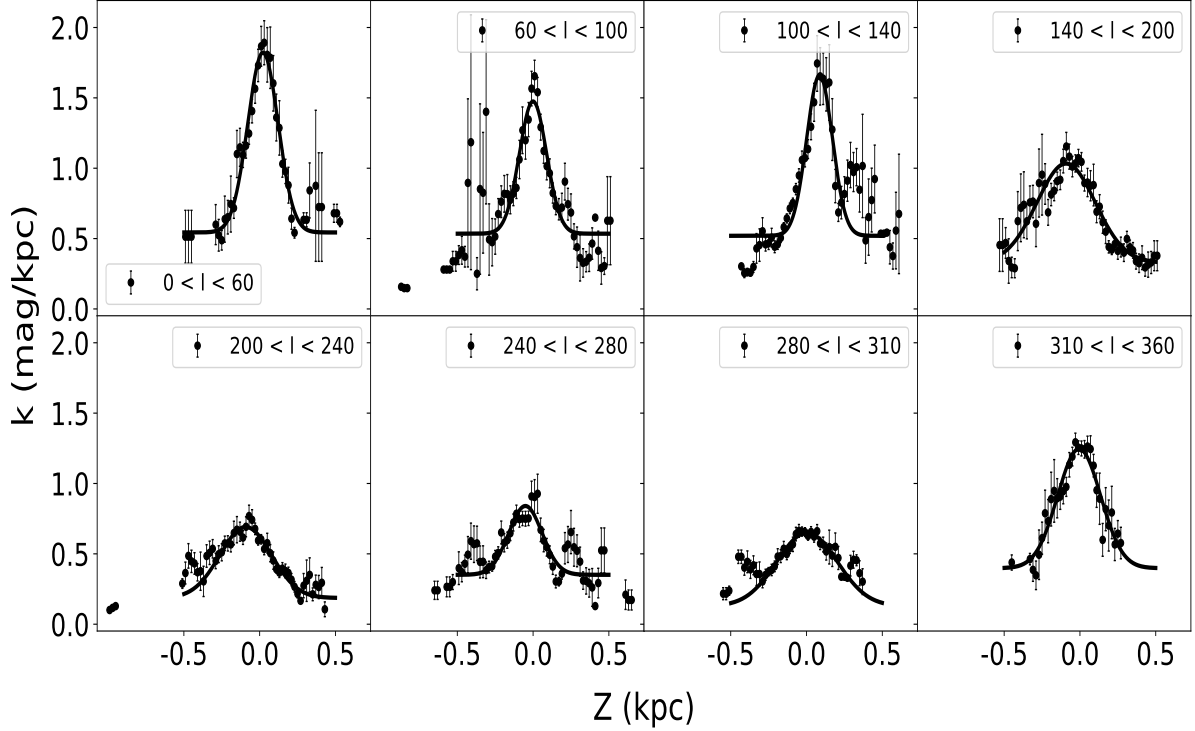


Figure 12: The variation of k as a function of z for 8 different regions in longitude. A least square Gaussian fit in the distribution is also drawn and resultant mean values are given at the top of each panel.

Table 3: Parameters obtained from the Gaussian fits in the 8 longitudinal zones. Here, k_0 , z_0 , and β represent maximum value of absorption, corresponding distance from the Galactic plane, and thickness of the absorbing material.

Longitude range (deg)	Number of open clusters	k_0 (mag/kpc)	ek_0 (mag/kpc)	z_0 (pc)	ez_0 (pc)	β (pc)	$e\beta$ (pc)
0 - 60	363	1.8	0.1	21.7	3.9	141.7	9.5
60 - 100	399	1.5	0.1	-0.5	5.6	127	10.9
100 - 140	470	1.7	0.1	86.1	4.8	120.3	8.9
140 - 200	374	1	0.1	-91.3	8.9	272.9	22
200 - 240	398	0.7	0.1	-92	6.1	240.3	22.7
240 - 280	453	0.8	0.1	-50.7	8.5	155.4	24.7
280 - 310	409	0.6	0.2	3.1	5.2	282	65.2
310 - 360	406	1.2	0.1	-5.3	6.5	200.6	20.4

The above equation shows that our view due to high reddening is most obscured in the direction of $l \sim 60^\circ \pm 5^\circ$ and least affected in $l \sim 240^\circ \pm 5^\circ$ where it reaches its minimum value of ~ 0.13 mag kpc $^{-1}$. A similar behaviour was also noticed by [Chen et al. \(1998\)](#) and [Joshi \(2005\)](#).

5.3. Normalized Galactic absorption

We determined the normalized interstellar absorption k as

$$k = \frac{A_v}{d} = R_v \frac{E(B - V)}{d}$$

where R_v is the total-to-selective absorption which is considered to be 3.1 for the normal dust-to-gas ratio. Here, we would like to remind that we have considered only those clusters for which R_v has a tolerance limit of 30% around the normal value of R_v . In order to study the concentration of reddening material in the Galactic mid-plane, the sky was divided into 8 zones of Galactic longitude. Since Galactic extinction varies in a non-uniform manner across the sky so does the number of observed

OCs. Hence, the zones cannot be made of uniform size. In our analysis, we chose zone size in such a way that the number of clusters in these zones is more or less similar. Figure 12 provides the distribution of interstellar absorption k as a function of z for all 8 zones. The Gaussian profile is fitted around the maximum absorption in each zone and estimates of the maximum value of absorption k_0 , corresponding distance from the Galactic plane z_0 , and half-width value β have been obtained for all the zones. All the parameters obtained from the best fit Gaussian profile are given in Table 3. The general pattern obtained from these zones provides a broad picture of the reddening material in the Galactic disk. The correlation of various parameters with the Galactic longitude is studied in the following analysis.

5.3.1. Variation in height z_0 at maximum absorption with longitude

To study the variation of maximum Galactic absorption perpendicular to the Galactic plane, we plotted the value of z_0 against the mean value of longitude in Figure 13. A least square solution

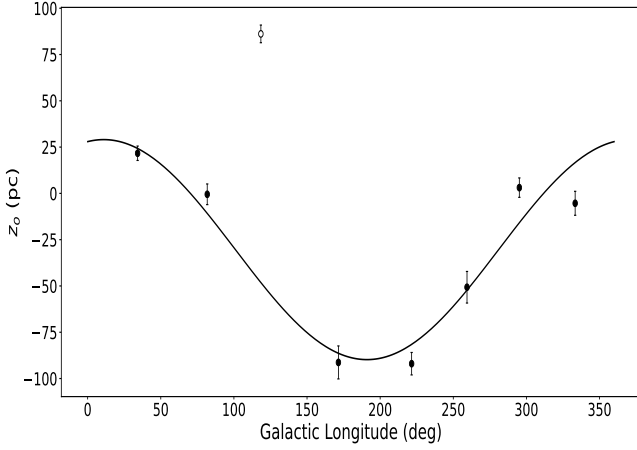


Figure 13: The height z above or below the Galactic plane at the maximum absorption k_0 as a function of Galactic longitude. The least-square sinusoidal fit is drawn by a continuous line. The point shown by an open circle is not included in the fit.

for a sinusoidal function gives

$$z_0 = -30.4 + 59.4 \sin(l + 79) \\ \pm 6.8 \pm 9.7 \quad \pm 9$$

Here we have excluded the point shown by the open circle during the least squares fit. The best fit shows that the distance of the Galactic plane at maximum absorption is symmetric around $z \sim -30 \pm 7$ pc which means that the reddening plane is lying below by the same value to the formal Galactic plane. This suggests that a higher proportion of the interstellar medium comprising of gas and dust is present below the Galactic plane and the Sun lies about 30 ± 7 pc above the reddening plane. The sinusoidal nature of variation of z_0 with Galactic longitude l signifies that the reddening plane is tilted with respect to the formal Galactic plane and this tilt is maximum in the direction of $11^\circ \pm 9^\circ$ Galactic longitude. The solar offset value determined on the basis of the reddening plane is higher in comparison to the same using the number density distribution of the clusters as derived in Section 4, however, within the broad range of solar offset values given in Karim & Mamajek (2017).

5.3.2. Variation in maximum Galactic absorption with longitude

As we have already seen, the absorption is minimum in the anti-center direction and reaches its maximum in the direction of the Galactic center which is populated by dense regions of gas and dust. To study this variation in greater detail, we draw the variation of k_0 as a function of the mean value of longitude which is illustrated in Figure 14. The variation seems to be sinusoidal in nature and a least squares solution to the absorption variation over the Galactic longitudes gives

$$k_0 = 1.23 + 0.5 \sin(l + 31) \\ \pm 0.06 \pm 0.07 \quad \pm 10$$

The absorption is therefore found to be maximum towards $l \sim 59^\circ \pm 10^\circ$ and it is minimum in the direction of $l \sim 239^\circ \pm 10^\circ$. It is similar to our earlier estimate in § 5.2.

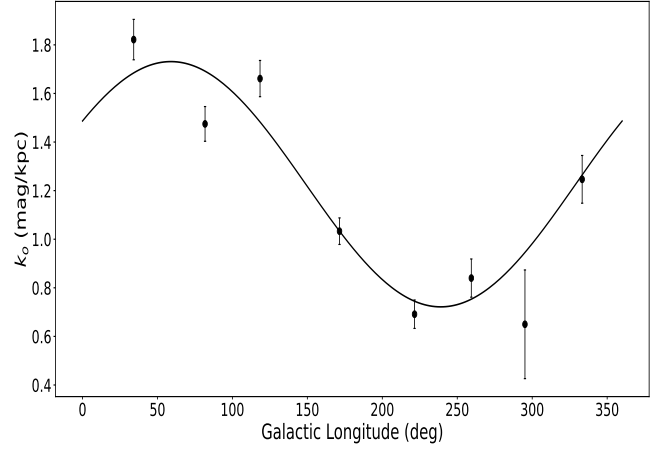


Figure 14: Maximum absorption k_0 as a function of Galactic longitude. A least square sinusoidal fit is drawn by a continuous line.

5.3.3. Thickness of the reddening plane

The thickness of the reddening plane is defined by the half-width value, β , of the Gaussian distribution which is estimated as the half of the separation between the z values at $1/e$ times the maximum value of the interstellar absorption (Neckel 1966; Pandey & Mahra 1987). We estimated β for each zone and have drawn them in Figure 15 as a function of mean Galactic longitude. It is quite evident that the thickness of the reddening material varies from ~ 120 to ~ 280 pc with maximum and minimum thickness lie in the regions of 250° and 70° of the Galactic longitude, respectively. The variation in the thickness of the reddening plane is a sinusoidal variation, as can be seen in Figure 15. β was obtained to vary about 204 ± 14 pc. The correlation between the thickness of the dust layer and the direction of the maximum reddening in the reddening plane is quite obvious. While β is relatively low in the direction of high reddening, it is relatively high in the direction of lower reddening. This shows that the concentration of interstellar material is more where the thickness of the reddening plane is narrow while the concentration of material is less where the thickness of the reddening plane is broad. The distribution of interstellar reddening material within a few kiloparsecs of the sun has also been studied by Fitzgerald (1968) and Pandey & Mahra (1987). While the former found β varying from 40 to 100 pc, later obtained it in between 50 to 210 pc. In our previous study in Joshi (2005) using 722 OCs, we found the mean value of β as 125 ± 21 pc, however, all these three studies used a smaller sample of OCs.

5.3.4. Inclination between reddening plane and Galactic plane

As we have observed earlier, the reddening plane defined by the plane of symmetry of reddening material is not only rotated about Galactic latitude but also rotated about Galactic longitude. To determine the inclination angle between the reddening plane and normal Galactic mid-plane, we investigated the distribution of z in a bin-width of 500 pc as a function of the heliocentric distance d (kpc) in Figure 16. We follow the methodology suggested by Fernie (1968) where we take the distances in the direction of maximum upward tilt i.e. $l \sim 11^\circ \pm 35^\circ$ as positive and negative in the direction of maximum downward tilt i.e. $l \sim 191^\circ \pm 35^\circ$ as estimated in Section 5.3.1. We fitted the data

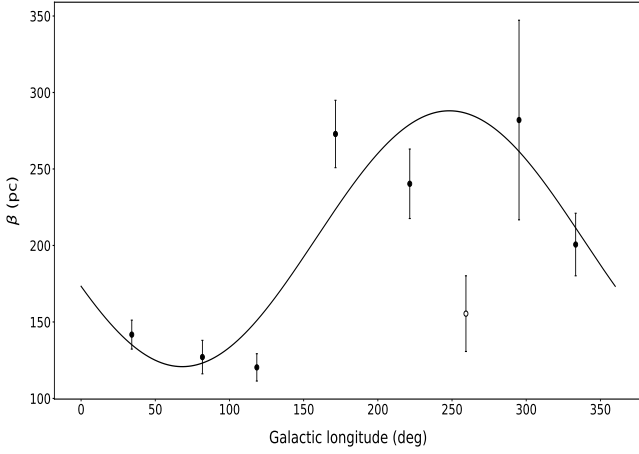


Figure 15: The half-width β of the Gaussian distribution which denotes the thickness of the reddening plane, as a function of Galactic longitude. The least-square sinusoidal fit is drawn by a continuous line. The point shown by an open circle is not included in the fit.

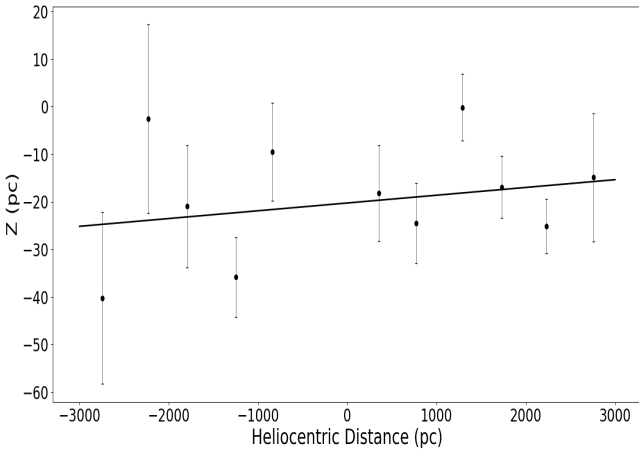


Figure 16: Mean value of the z as a function of distance in the direction of $l = 11^\circ \pm 35^\circ$ (taken as a positive distance) and $l = 191^\circ \pm 35^\circ$ (taken as a negative distance). The least squares fit for the sample restricted to $(-3.0, 3.0)$ kpc is shown by a continuous line which gives an inclination angle $\phi = 0.1^\circ \pm 0.1^\circ$.

with a straight line of the form,

$$z = z_{\odot} + d \sin(\phi)$$

where z_{\odot} is the offset of the reddening plane from the Galactic plane at the solar position and ϕ is the angle of inclination between the two planes. A least squares fit yields $\phi = 0.1^\circ \pm 0.1^\circ$ and $z_{\odot} = -20.3 \pm 4.0$ pc. Our value of inclination angle is smaller than that found in many previous studies and we also see a lot of scatters in the $d - z$ plane. Fernie (1968) has examined Galactic Cepheids which have a typical age range between 20 to 700 Myr and obtained this tilt as $\phi = 0.8^\circ \pm 0.2^\circ$ for the Cepheids population. Using a smaller sample of 462 OCs, Pandey & Mahra (1987) found that the reddening plane is inclined to the formal Galactic plane by an angle of $0.2^\circ \pm 0.6^\circ$ and showed a maximum upward tilt towards $l \sim 60^\circ$ which is close to our present estimate. From the sample of 722 OCs, Joshi (2005) found the inclination value as $0.6^\circ \pm 0.4^\circ$.

5.4. Cluster scale height from the reddening plane

The observed clusters distribution perpendicular to the Galactic plane provides us with an estimate of the thickness of the young Galactic disk. In a similar manner, we plan to estimate the thickness of the reddening plane by obtaining scale height from the reddening plane which is defined by Fernie (1968) as follows:

$$z' = z_{\odot} + d \sin b \cos \phi - d \cos b \sin \phi \cos(l - \theta_t)$$

where z_{\odot} is the solar offset, ϕ is the inclination angle obtained in the previous section and θ_t is the angle of maximum inclination of the reddening plane with respect to the normal Galactic plane the value of which was derived previously as $11^\circ \pm 9^\circ$ in Section 5.3.1. We fitted the number distribution of OCs in the exponential profile described in Eq. (1) to estimate the scale height as shown in Figure 17. The scale height of the distribution of clusters in the reddening plane is found to be $z'_h = 101.3 \pm 2.0$ pc. If we consider only young clusters having ages $T < 700$ Myr, we find a smaller scale height of $z'_h = 89.6 \pm 2.6$ pc. Pandey & Mahra (1987) reported a scale height of 160 ± 20 pc for the distribution of reddening material which is substantially larger than the present estimate.

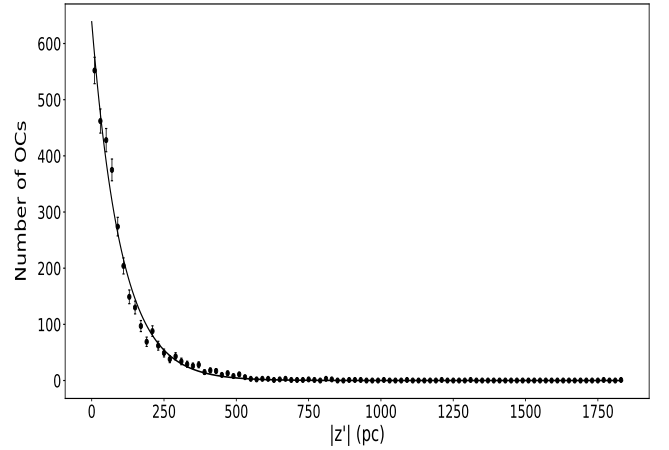


Figure 17: $|z'|$ distribution of OCs along with the least square exponential decay profile fit shown by a continuous line. The error bars shown in the y-axis are the Poisson errors.

6. Discussion and Summary

In this work, we compiled various catalogs of Galactic OCs that became available recently and found a total of 6133 OCs, most of which have been detected in the post-Gaia phase using the photometric and kinematic information provided in the Gaia archive data. We used the position, distance, age, and kinematic parameters of these clusters to study the Galactic disk morphology. The ages of OCs cover a whole range, from a few Myrs to tens of billions of years, making them excellent tracers for investigating the Galactic disk, spiral structure, and in particular the evolution of spiral arms. Though our cluster sample seems to be complete only up to 2 kpc from the Sun but clusters are found to be located as far as 13 kpc from the Solar position. The distribution of our sample of OCs in the $X - Y$ plane clearly showed signatures of the spiral arms particularly when we only considered clusters younger than 30 Myrs as older OCs have a more scattered distribution. In the spiral arms and inter-arm regions, the distributions

of OCs reveal the complex substructures in the spiral arms. By analysing young clusters in different age bins, we could delineate the spiral structures and found that clusters start leaving the spiral arms after 10–20 Myrs and fill the inter-arm regions where they stay for the rest of their life. The two spiral structures related to the Local arm and Scutum-Centaurus spiral arms were conspicuous by their presence while some substructures of Perseus and Scutum-Centaurus spiral arms were feebly present. Once we were able to trace the spiral arms using the younger clusters, we went on to study their pattern speed by making use of the 3D kinematic data of OCs adopting the methodology given by [Dias & Lépine \(2005\)](#). We found that the rotational pattern speeds were almost similar for all spiral arms within 1σ , which showed no acceleration in the last 80 Myrs. The constant pattern speed across the spiral arms suggests the rigid body motion of the spiral arms which is in contrast to the study by [Castro-Ginard et al. \(2021\)](#) who obtained that the rotational speed of spiral arms decreases with the distance closely following the rotation curve of the Milky Way. In our study we used a larger catalog of about 440 OCs and deduced the mean spiral arm pattern speed to be $\Omega = 26.5 \pm 1.5 \text{ km s}^{-1} \text{ kpc}^{-1}$ thereafter finding the corotation radius to be close to the solar orbit at $\sim 9 \text{ kpc}$ which can explain the gap in the distribution of OCs at about the same distance from the Galactic centre. The number density distribution of OCs has been used to determine the Solar offset and scale height which are found to be about $-17.0 \pm 0.9 \text{ pc}$ and $91.7 \pm 1.9 \text{ pc}$, respectively considering clusters younger than 700 Myrs. However, we found these numbers vary when we alter the selection criteria of the chosen cluster sample.

We further carried out a study of the distribution of interstellar material in the Galactic disk at the lower latitudes. The sample of OCs having reddening information, which was used here, has increased significantly from 722 to 4233, almost six times, from the last such study carried out in [Joshi \(2005\)](#). We found that most of the reddening material resides close to the Galactic plane and reddening decreases as z increases on either side of the mid-plane. It is found from the extinction distribution of OCs that about 90% of the absorbing material lies within $-10^\circ \leq b \leq 10^\circ$ of the Galactic mid-plane. We noticed that the interstellar absorption normalized with the cluster distance follows a sinusoidal variation with the Galactic longitude and absorption is minimum in the anti-center direction and reaches its maximum in the direction of the Galactic center which is populated by the dense regions of gas and dust. The maximum and minimum absorption are found to be at respective longitudinal directions of $\sim 59^\circ \pm 10^\circ$ and $\sim 239^\circ \pm 10^\circ$. Moreover, a higher proportion of the interstellar material comprising gas and dust seems to be present below the Galactic plane. We also observed that the Galactic plane defined by the reddening material is not co-planar with the formal Galactic plane but inclined by an angle of $\sim 0.1^\circ \pm 0.1^\circ$ to the Galactic mid-plane and this tilt is maximum in the longitudinal directions of $\sim 11^\circ$. The mean thickness of the absorbing material in the reddening plane, as determined in terms of half-width value β , is estimated to be about $204 \pm 14 \text{ pc}$. We found a scale height of $101.3 \pm 2.0 \text{ pc}$ for the distribution of reddening material which is slightly larger in comparison to the distribution of OCs around the Galactic mid-plane.

Acknowledgments

SM would like to thank ARIES to provide support through its Visiting Student Program (VSP) to conduct his master's thesis project. This work has made use of data from the European Space Agency (ESA) mission

Gaia (<https://www.cosmos.esa.int/gaia>), processed by the Gaia Data Processing and Analysis Consortium (DPAC, <https://www.cosmos.esa.int/web/gaia/dpac/consortium>).

References

- Amôres, E. B., Lépine, J. R. D., & Mishurov, Y. N. 2009, *MNRAS*, 400, 1768
 Barros, D. A., Lépine, J. R. D., & Junqueira, T. C. 2013, *MNRAS*, 435, 2299
 Bonatto, C., Kerber, L. O., Bica, E., & Santiago, B. X. 2006, *A&A*, 446, 121
 Bovy, J. 2015, *ApJS*, 216, 29
 Buckner, A. S. M., & Froebrich, D. 2014, *MNRAS*, 444, 290
 Cambrésy, L., Jarrett, T. H., & Beichman, C. A. 2005, *A&A*, 435, 131
 Cantat-Gaudin, T., & Anders, F. 2020, *A&A*, 633, A99
 Cantat-Gaudin, T. et al. 2020, *A&A*, 640, A1
 Cantat-Gaudin, T. et al. 2018, *A&A*, 618, A93
 Cantat-Gaudin, T. et al. 2019, *A&A*, 624, A126
 Castro-Ginard, A., Jordi, C., Luri, X., Cantat-Gaudin, T., & Balaguer-Núñez, L. 2019, *A&A*, 627, A35
 Castro-Ginard, A. et al. 2022, *A&A*, 661, A118
 Castro-Ginard, A. et al. 2021, *A&A*, 652, A162
 Chen, B., Figueras, F., Torra, J., Jordi, C., Luri, X., & Galadí-Enríquez, D. 1999, *A&A*, 352, 459
 Chen, B., Vergely, J. L., Valette, B., & Carraro, G. 1998, *A&A*, 336, 137
 Chen, B. Q. et al. 2014, *MNRAS*, 443, 1192
 Chen, Y. Q., & Zhao, G. 2020, *MNRAS*, 495, 2673
 Cohen, M. 1995, *ApJ*, 444, 874
 de la Fuente Marcos, R., & de la Fuente Marcos, C. 2004, *New A*, 9, 475
 Dias, W. S., & Lépine, J. R. D. 2005, *ApJ*, 629, 825
 Dias, W. S., Monteiro, H., Caetano, T. C., Lépine, J. R. D., Assafin, M., & Oliveira, A. F. 2014, *A&A*, 564, A79
 Dias, W. S., Monteiro, H., Lépine, J. R. D., & Barros, D. A. 2019, *MNRAS*, 486, 5726
 Dias, W. S., Monteiro, H., Moitinho, A., Lépine, J. R. D., Carraro, G., Paunzen, E., Alessi, B., & Vilella, L. 2021, *MNRAS*, 504, 356
 Dobbs, C. L., Bending, T. J. R., Pettitt, A. R., Buckner, A. S. M., & Bate, M. R. 2022, *MNRAS*, 517, 675
 Fernie, J. D. 1968, *AJ*, 73, 995
 Fitzgerald, M. P. 1968, *AJ*, 73, 983
 Gaia Collaboration et al. 2018, *A&A*, 616, A1
 Gaia Collaboration et al. 2016, *A&A*, 595, A2
 Gerhard, O. 2011, *Memorie della Societa Astronomica Italiana Supplementi*, 18, 185
 Griv, E., Gedalin, M., & Jiang, I.-G. 2022, *MNRAS*, 512, 1169
 Guo, H. L. et al. 2021, *ApJ*, 906, 47
 Hao, C. J. et al. 2021, *A&A*, 652, A102
 Hao, C. J., Xu, Y., Wu, Z. Y., Lin, Z. H., Liu, D. J., & Li, Y. J. 2022, *A&A*, 660, A4
 He, Z.-H., Xu, Y., Hao, C.-J., Wu, Z.-Y., & Li, J.-J. 2021, *Research in Astronomy and Astrophysics*, 21, 093
 Hou, L. G. 2021, *Frontiers in Astronomy and Space Sciences*, 8, 103
 Joshi, Y. C. 2005, *MNRAS*, 362, 1259
 Joshi, Y. C. 2007, *MNRAS*, 378, 768
 Joshi, Y. C., Dambis, A. K., Pandey, A. K., & Joshi, S. 2016, *A&A*, 593, A116
 Karim, T., & Mamajek, E. E. 2017, *MNRAS*, 465, 472
 Liu, L., & Pang, X. 2019, *ApJS*, 245, 32
 Majaess, D. J., Turner, D. G., & Lane, D. J. 2009, *MNRAS*, 398, 263
 Monteiro, H., Barros, D. A., Dias, W. S., & Lépine, J. R. D. 2021, *Frontiers in Astronomy and Space Sciences*, 8, 62
 Neckel, T. 1966, *ZAp*, 63, 221
 Pandey, A. K., & Mahra, H. S. 1987, *MNRAS*, 226, 635
 Poggio, E. et al. 2021, *A&A*, 651, A104
 Reid, M. J. et al. 2019, *ApJ*, 885, 131
 Ryu, J., & Lee, M. G. 2018, *ApJ*, 856, 152
 Sakai, N., Nakanishi, H., Kurahara, K., Sakai, D., Hachisuka, K., Kim, J.-S., & Kameya, O. 2022, *PASJ*, 74, 209
 Sharma, S., Pandey, A. K., Ojha, D. K., Chen, W. P., Ghosh, S. K., Bhatt, B. C., Maheswar, G., & Sagar, R. 2007, *MNRAS*, 380, 1141
 Siebert, T. 2019, *A&A*, 632, L1
 Sim, G., Lee, S. H., Ann, H. B., & Kim, S. 2019, *Journal of Korean Astronomical Society*, 52, 145
 Tarricq, Y. et al. 2021, *A&A*, 647, A19
 Yao, J. M., Manchester, R. N., & Wang, N. 2017, *MNRAS*, 468, 3289
 Zhang, H., Chen, Y., & Zhao, G. 2021, *ApJ*, 919, 52
 Zhong, J., Chen, L., Jiang, Y., Qin, S., & Hou, J. 2022, *AJ*, 164, 54